

Exchange magnon-polaritons in microwave cavities

Yunshan Cao¹, Peng Yan¹, Hans Huebl^{2,3,4}, Sebastian T.B. Goennenwein^{2,3,4}, and Gerrit E.W. Bauer^{5,1}

¹*Kavli Institute of NanoScience, Delft University of Technology, Lorentzweg 1, 2628 CJ Delft, The Netherlands*

²*Walther-Meißner-Institute, Bayerische Akademie der Wissenschaften, 85748 Garching, Germany*

³*Nanosystems Initiative Munich, D-80799 München, Germany*

⁴*Physik-Department, Technische Universität München, D-85748 Garching, Germany and*

⁵*Institute for Materials Research and WPI-AIMR, Tohoku University, Sendai 980-8577, Japan*

(Dated: August 20, 2018)

We formulate a scattering theory to study magnetic films in microwave cavities beyond the independent-spin and rotating wave approximations of the Tavis-Cummings model. We demonstrate that strong coupling can be realized not only for the ferromagnetic resonance (FMR) mode, but also for spin wave resonances (SWRs); the coupling strengths are mode dependent and decrease with increasing mode index. The strong coupling regime can be also accessed electrically by spin pumping into a metal contact.

PACS numbers: 75.30.Ds, 75.60.Ch, 85.75.-d

I. INTRODUCTION

Strong light-matter interaction is a central subject in quantum information and communication science and technology. Hybrid systems consisting of resonantly coupled spin ensembles and microwaves received much attention recently [1–3]. In magnetic materials, spins are coupled by the exchange interactions into ordered states. The collective elementary excitations of the spin system are spin waves or magnons. Arguably the most important experimental technique is the microwave spectroscopy of the magnetic order parameter called ferromagnetic resonance (FMR) and/or spin wave resonance (SWR) [4], which is usually used to study magnetism in the weak coupling limit. In the strong coupling limit, the hybridized states of the magnetic order parameter with electromagnetic waves are magnon-polaritons [5, 6]. They can be observed only when the viscous damping of the magnetization dynamics as parameterized by the Gilbert constant is sufficiently weak. Of special interest from a materials perspective is yttrium iron garnet (YIG) [7, 8], a ferrimagnetic insulator. YIG is advantageous due to (i) an extremely low dissipation, with Gilbert damping factor α down to $\sim 10^{-5}$ [9]; (ii) a large spin density $2 \times 10^{22} \text{ cm}^{-3}$ [10], much higher than in paramagnetic materials which only have about $10^{15} \sim 10^{18} \text{ cm}^{-3}$ [11, 12]. Therefore, strong coupling is much easier to achieve using YIG, in either broad-band coplanar waveguides (CPWs) [13–15] or metallic microwave cavities [16–18].

The conventional description for the coherent interaction between spins and photons is based on the Tavis-Cummings (TC) model [19], where the effective coupling strength $g_{\text{eff}} = \sqrt{N}g_s$ of a single magnon (N spins) to a single photon is enhanced by \sqrt{N} as compared to the coupling g_s to a single spin. A standard input-output formalism in the low photon number limit [20, 21] provides the transmission amplitude of microwaves from the input to the output port of the microwave resonator (sketched in Fig. 1(a)),

$$S_{21} = \frac{\kappa_c}{i(\omega - \omega_c) - (\kappa_e + \kappa_i) + \Sigma(\omega)}, \quad (1)$$

where $\omega_c, \kappa_{e,i}$ are, respectively, the resonance frequency and

external/intrinsic loss rates of the microwave resonator (total damping rate $\kappa_c = \kappa_e + \kappa_i$). The self-energy caused by the magnon-photon coupling reads $\Sigma(\omega) = g_{\text{eff}}^2 / [i(\omega - \omega_{\text{FMR}}) - \kappa_s]$, with FMR frequency ω_{FMR} and magnetic relaxation rate κ_s . When $g_{\text{eff}} > \kappa_{s,c}$, the strong coupling regime is achieved and explained well by the TC model [11–19]. However, the TC model based on monochrome mode interaction and the rotating-wave approximation (RWA), fails to describe the ultra-strong coupling (USC) regime and multi-mode behavior. Although the TC model can in principle be repaired to cover the USC regime [22], the cited experiments investigated ferromagnetic samples of different shapes exposed to microwaves in different geometries, which is beyond a generic TC model. In this paper we present a first-principles theory that supersedes the TC model in treating ferromagnetic objects coherently interacting with microwaves.

Huebl *et al.* [13] demonstrated strong coupling of a YIG film in a superconducting CPW in terms of an anti-crossing in the microwave transmission spectrum when the FMR matches the CPW frequency. A series of anti-crossings for thicker YIG samples indicative of spin wave excitations are reported in YIG-film split-rings [14, 15]. Tabuchi *et al.* [16] studied the strong coupling regime for YIG spheres in 3D cavity system down to low temperatures and subsequently coupled the magnon to a qubit via the microwave cavity mode. Characteristic phenomena associated with distinct parameter regimes, like magnetically induced transparency ($\kappa_s < g_{\text{eff}} < \kappa_c$) and Purcell effect ($\kappa_c < g_{\text{eff}} < \kappa_s$), even the USC regime beyond the RWA were observed by Zhang *et al.* [17]. Goryachev *et al.* [18] reported strong coupling between multiple magnon modes and a dark cavity mode for submillimeter-size YIG spheres in 3D reentrant cavities, as well as a high cooperativity of $> 10^5$ by USC to a bright cavity mode.

Strongly hybridized magnon-polaritons as observed in the above experiments cannot be described in terms of a single magnon-photon coupling process. In the present work, we formulate the coupling of a magnetic film to microwaves in a cavity by means of scattering approach. Our method is valid for the full parameter range spanning the weak to strong, even

ultra-strong coupling limits. We obtain a general transmission formula that reduces to the TC model in the appropriate limits. To this end we solve the coupled Maxwell's and Landau-Lifshitz-Gilbert (LLG) equations without making the conventional magnetostatic approximation. We may then compute microwave absorption and transmission spectra that can be characterized by multi-mode strong coupling and the mode-dependent coupling strengths. Furthermore, we consider the electric detection in the strong coupling regime through spin pumping [23] technique as measured in a Pt contact by the inverse spin Hall effect (ISHE) [24, 25].

This paper is organized as follows: In Sec. II, we model the cavity and derive the equations of motion for coupled magnons and photons. Section III gives the formulation of the scattering theory and the main results of the magnon-photon strong coupling in both paramagnets and ferromagnets. An electric detection of the strong coupling is also proposed via spin pumping and inverse spin Hall effects. Conclusions are drawn in Sec. IV.

II. MODEL

The weak to strong coupling transition can best be studied in a simple configuration as shown in Fig. 1(a). The calculations for general configurations will be reported elsewhere. The magnetic film lies in the y - z plane between the cavity defining mirrors. The equilibrium magnetization points into the z -direction by crystal anisotropy, dipolar, and external magnetic fields. The incident microwave propagates along x with rf magnetic field linearly polarized along y . The cavity walls are modeled by the permeability $\mu(x) = \mu_0 [1 + 2\ell\delta(x) + 2\ell\delta(x - L)]$, where L is the cavity width and ℓ models the wall opacity. In the absence of sources, the microwaves satisfy the Maxwell's equation in frequency space,

$$\partial_x^2 \mathbf{h}(x) + \frac{\mu(x)}{\mu_0} q^2 \mathbf{h}(x) = 0, \quad (2)$$

where $q = \omega/c$, with vacuum speed of light $c = 1/\sqrt{\varepsilon_0\mu_0}$, and ε_0, μ_0 are the vacuum permittivity and permeability, respectively.

Inside the magnetic film, we consider small-amplitude spatiotemporal magnetizations $\mathbf{M} = M_s \hat{z} + \mathbf{m}$, where M_s is the saturation magnetization and \mathbf{m} is driven by the rf magnetic field \mathbf{h} , according to the Maxwell's equation

$$(\nabla^2 + k_\varepsilon^2) \mathbf{h}(x) = \nabla(\nabla \cdot \mathbf{h}(x)) - k_\varepsilon^2 \mathbf{m}(x), \quad (3)$$

where ε is the permittivity of the magnet, $k_\varepsilon^2 \equiv \varepsilon\mu_0\omega^2 = \eta q^2$, and dielectric constant $\eta = \varepsilon/\varepsilon_0$. \mathbf{M} is governed by the LLG equation,

$$\partial_t \mathbf{M} = -\gamma\mu_0 \mathbf{M} \times \mathbf{H}_{\text{eff}} + \frac{\alpha}{M_s} \mathbf{M} \times \partial_t \mathbf{M}, \quad (4)$$

where γ, α are the gyromagnetic ratio and Gilbert damping constant, respectively. The effective magnetic field $\mathbf{H}_{\text{eff}} = H\hat{z} + \mathbf{H}_{\text{ex}} + \mathbf{h}$, consists of external, exchange, and rf magnetic

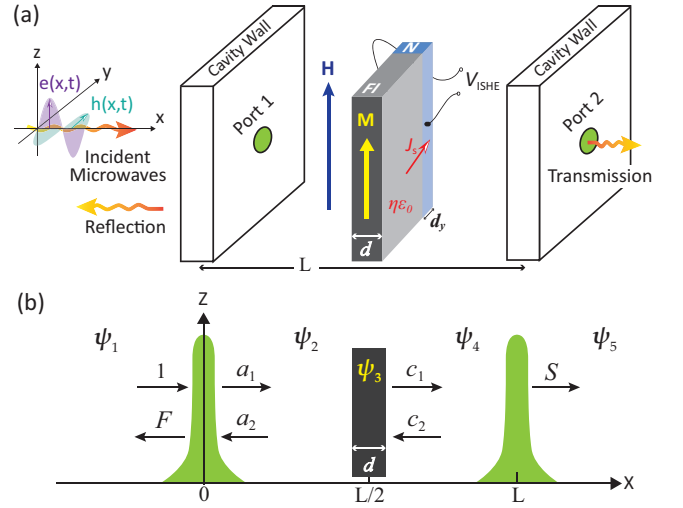


FIG. 1. Magnetic film in a planar microwave cavity.

fields, where, the exchange field $\mathbf{H}_{\text{ex}} = J\nabla^2 \mathbf{m}$ with exchange constant J . For wave vector $\mathbf{k} = k\hat{x}$, the coupled Eqs. (3) and (4) become,

$$\begin{pmatrix} (1 + u_k)k_\varepsilon^2 & -iv_k k_\varepsilon^2 \\ iv_k k_\varepsilon^2 & (1 + u_k)k_\varepsilon^2 - k^2 \end{pmatrix} \begin{pmatrix} h_x \\ h_y \end{pmatrix} = 0. \quad (5)$$

with $\omega_M = \gamma\mu_0 M_s$, $\omega_H = \gamma\mu_0 H$, $\omega_k = \omega_H + J\omega_M k^2 - i\alpha\omega$ and

$$u_k = \frac{\omega_k \omega_M}{\omega_k^2 - \omega^2}, \quad v_k = \frac{\omega \omega_M}{\omega_k^2 - \omega^2}. \quad (6)$$

The secular equation of Eq. (5) gives the dispersion relation for the coupled microwave and spin wave modes or magnon-polaritons [26–28]

$$(1 + u_k)k^2 = [(1 + u_k)^2 - v_k^2]k_\varepsilon^2. \quad (7)$$

III. RESULTS

A. Paramagnet ($J = 0$)

We first consider the simplest case of a paramagnet with uncoupled spins ($J = 0$), which is equivalent with the macrospin model for unpinned ferromagnetic order. $u_k = u, v_k = v$ are k independent and $k = k_\varepsilon \sqrt{1 + u - v^2/(1 + u)}$ for a given frequency ω . $h_x = -m_x$ is the dipolar field. The susceptibility $\chi = \partial m_y / \partial h_y$ resonates at $\omega_{\text{FMR}} = \sqrt{\omega_H(\omega_H + \omega_M)}$ with linewidth $\Delta\omega_{\text{FMR}} \approx \alpha(2\omega_H + \omega_M)$. Rewriting the $h_y(x, t) = \psi(x)e^{-i\omega t}$, the potentials $\psi(x)$ in the five separated regimes marked in Fig.1(b) read

$$\psi_1(x) = e^{iqx} + F e^{-iqx}, \quad \psi_2(x) = a_1 e^{iqx} + a_2 e^{-iqx}, \quad (8a)$$

$$\psi_3(x) = b_1 e^{ikx} + b_2 e^{-ikx}, \quad \psi_4(x) = c_1 e^{iqx} + c_2 e^{-iqx}, \quad (8b)$$

$$\psi_5(x) = S e^{iqx}. \quad (8c)$$

The coefficients $\{S, F, a_1, a_2, b_1, b_2, c_1, c_2\}$ are determined by the electromagnetic boundary conditions of continuity and flux conservation at each interface. The transmission coefficient is

$$S = \frac{(1 - \beta^2) t_c^2 e^{i(k-q)d}}{(1 - \beta r_c e^{i\phi})^2 - e^{2ikd} (\beta - r_c e^{i\phi})^2}, \quad (9)$$

where $\phi = q(L - d)$, $\beta = (\eta q - k)/(\eta q + k)$, introducing the scattering coefficients of a single cavity wall $t_c = i/(i + q\ell)$ and $r_c = -q\ell/(i + q\ell)$. We first inspect the resonant cavity modes identified by the maxima of the transmission probability $|S|^2$ for non-magnetic loads at

$$(1 + |r_c|^2) \beta \sin(kd) = |r_c| \left[\beta^2 \sin(kd - \phi^*) + \sin(kd + \phi^*) \right], \quad (10)$$

where $\phi^* = \phi + \text{Arg}(r_c)$. For $d = 0$, we recover the resonance condition of an empty cavity: $\phi_n^* = (n + 1)\pi$, with mode index $n = 1, 2, \dots$. It follows from Eqs. (7) and (10) that the resonance frequencies $\omega_{c,n}$ depend on both loading fraction d/L and dielectric constant η . The cavity mode frequencies for a nonmagnetic load are shown in Fig. 2(a). Odd modes $\omega_{c,2j-1}$ have nodes of the electric field at the sample position and depend only weakly on the film thickness, in contrast to the even modes $\omega_{c,2j}$ with antinodes that lead to redshifts. The anti-crossings of the cavity modes indicate hybridization induced by the dielectric load that modulates its intrinsic properties. The mode shifting due to the dielectric loading predicted here is absent in the TC model. To avoid this complication, we focus our discussions on the nearly empty cavity regime with loading rates $d/L < 5\%$ and on odd cavity modes.

In the limit of long wavelength, i.e., $k \ll 1/d$ only the leading term up to order k^2 contributes. The transmission coefficient then reduces to

$$S_n = \frac{\kappa_{c,n}}{i(\omega - \omega_{c,n}) - \kappa_{c,n} - i g_n^2 (\omega - \omega_{\text{FMR}} + i \kappa_{s,n})^{-1}}, \quad (11)$$

where $\kappa_{c,n} \approx c^3/[2(L - d)\omega_{c,n}^2 \ell^2]$ is the loss rate of the loaded cavity, and $\kappa_{s,n} \approx \alpha \sqrt{\omega_M^2 + 4\omega_{c,n}^2}/2$ is that of the magnetic film to the leading order in the Gilbert damping α .

The effective coupling strengths g_n depend on the parity of the cavity modes, i.e., the odd-mode coupling scales as \sqrt{d}

$$g_{2j-1}^2 = \frac{d\omega_M(\omega_M + \omega_H)}{2(L - d)} \cos^2 \frac{\phi_{2j-1}^*}{2}, \quad (12a)$$

while for even modes higher order corrections have to be included

$$g_{2j}^2 = \frac{d\omega_M(\omega_M + \omega_H)}{2(L - d)} \cos^2 \frac{\phi_{2j}^*}{2} \times \left| 1 - d\eta q_{2j} \tan \frac{\phi_{2j}^*}{2} + \frac{(d\eta q_{2j} \tan(\phi_{2j}^*/2))^2}{6} \right|, \quad (12b)$$

where ϕ_n^* is the phase at resonance frequency $\omega_{c,n}$. Both odd and even modes can be tuned by the total number of spins

$\propto d$ and by the dielectric constant η . Anti-crossings between magnetic and cavity modes occur at $\omega_{\text{FMR}} = \omega_{c,n}$ or $\mu_0 H_{\text{res},n} = (-\omega_M + \sqrt{\omega_M^2 + 4\omega_{c,n}^2})/(2\gamma)$. When not stated otherwise, we use the parameters for YIG, with $\eta = 15$ [29], $\gamma/(2\pi) = 28$ GHz/T and $\mu_0 M_s = 175$ mT [30], while reported α 's range from $10^{-5} \sim 10^{-3}$ [9, 31, 32]. The resonance frequency ω_c and loss rate κ_c of the cavity is governed by its width L and opacity ℓ . We choose $L = 46$ mm to be much larger than the film thickness d and the $n = 3$ cavity mode (around 10 GHz) as well as a $\kappa_{c,3}$ of the order of MHz, both of which can be tuned by ℓ .

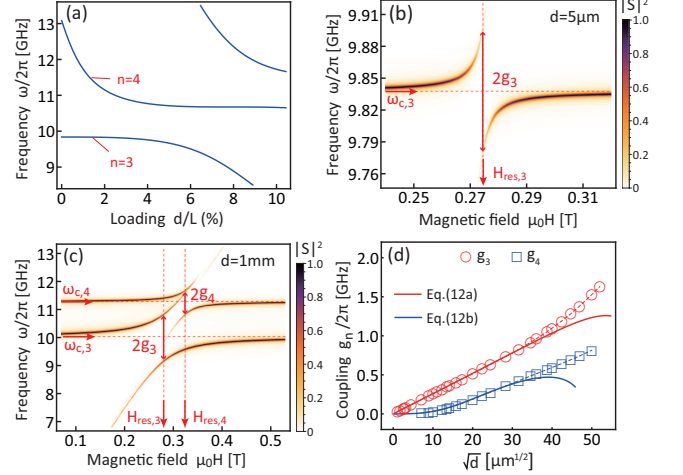


FIG. 2. (a) Hybridized cavity eigen-modes [solutions of Eq. (10)] in the presence of a non-magnetic load as a function of loading rate with dielectric constant $\eta = 15$. Transmission spectra as a function of magnetic field and frequency for two different magnetic films with parameters (b) $d = 5 \mu\text{m}$, and (c) $d = 1 \text{ mm}$. (d) Thickness dependence of coupling strength for the third and fourth modes. In the calculations, the length of the cavity $L = 46$ mm, cavity opacity $\ell/L = 2$ except for 0.4 used in (c) to demonstrate the USC with enough resolution, Gilbert damping $\alpha = 3 \times 10^{-4}$, and exchange constant $J = 0$ (paramagnetic limit).

The transmission spectrum in the paramagnetic limit $J = 0$ is shown for a thin film with $d = 5 \mu\text{m}$ ($d/L = 0.01\%$) in Fig. 2(b). At the resonant photon frequency $\omega_{c,3} = 9.84$ GHz, a coupling strength of $g_3 = 57.77$ MHz is extracted from the anti-crossing, where g_3 is much larger than both $\kappa_{c,3} = 1.44$ MHz and $\kappa_{s,3} = 3.04$ MHz, which implies strong coupling for a quasi 1D model assuming homogeneous crossing section. However, when $d = 1 \text{ mm}$ ($d/L = 2.17\%$) in Fig. 2(c), an additional anti-crossing resonance at $\omega_{c,4} = 11.27$ GHz is observed with coupling strength $g_4 = 0.43$ GHz. The main resonance for $\omega_{c,3} = 10.03$ GHz has a coupling strength $g_3 = 0.83$ GHz, corresponding to a cooperativity $C = g_3^2/(\kappa_c \kappa_s) = 15072$ at loss rates $\kappa_{c,3} = 34.71$ MHz and $\kappa_{s,3} = 3.10$ MHz, thereby approaching the USC regime of $g_n \geq 0.1\omega_{c,n}$. The coupling can also go into the magnetically-induced transparency and Purcell effect regimes [17] by tuning the parameters (not shown here).

The coupling strengths increase with \sqrt{d} as shown in Fig. 2(d), where the red circles and blue squares are extracted from numerical results for the full model calculations Eq. (9), and the solid lines are the analytical Eqs. (12a) and (12b) without any fitting parameter. In the paramagnetic limit, the full model converges to Eq. (1) when $kd \ll 1$. The formula for g_n begins to deviate when $kd \approx 1$, where film thickness $d \approx c/(\sqrt{\eta}\omega) = 1.3 \text{ mm}$ for $\omega/2\pi = 10 \text{ GHz}$ as shown in Fig. 2(d). Finite temperature can significantly reduce the spin polarization of paramagnets, while ferromagnets are much more robust.

B. Ferromagnet ($J > 0$)

Now we consider finite exchange coupling, i.e., $J > 0$. Equation (7) has then 3 solutions for a given frequency and $\psi_3(x)$ is modified as

$$\psi_3(x) = \sum_{j=1}^3 (b_{1,j} e^{ik_j x} + b_{2,j} e^{-ik_j x}). \quad (13)$$

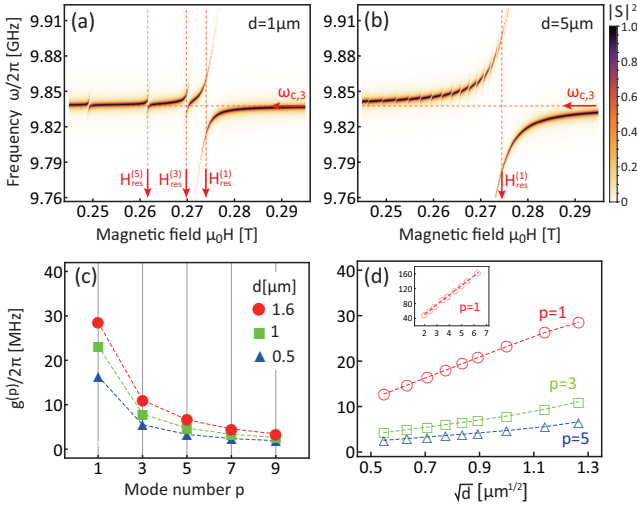


FIG. 3. (a,b) : Transmission for $d = 1 \mu\text{m}$ and $d = 5 \mu\text{m}$; (c,d): Mode-dependent coupling strengths. In the calculations we used cavity opacity $\ell/L = 2$, Gilbert damping $\alpha = 10^{-5}$, and ferromagnetic exchange constant $J = 3 \times 10^{-16} \text{ m}^2$ [8].

The magnetization dynamics now becomes sensitive to the surface boundary conditions. Kittel [33] has shown that pinning of the magnetization at the surface is required for SWR (the absorption of spatially homogeneous microwaves by higher order spin waves), and the symmetrically pinned boundaries merely render odd modes observable. Here we adopt boundary conditions $\mathbf{m}((L \pm d)/2) = 0$, which can be justified by sufficiently strong surface anisotropies [34, 35]. The standing spin wave frequencies are $\omega_{\text{SWR}}^{(p)} = \sqrt{(\omega_H + 2J\omega_M(p\pi/d)^2)(\omega_M + \omega_H + 2J\omega_M(p\pi/d)^2)}$ where $p \in \mathbb{N}_0$. We consider in the following magnetic film thicknesses in the range $0.1 \sim 5 \mu\text{m}$. Naively, exchange effects are

appreciable when the magnetic film thickness is comparable with the exchange length, $\lambda_{\text{ex}} \approx 17 \text{ nm}$ for YIG, but they play a significant role in the spectra of much thicker samples. For high quality magnetization dynamics corresponding to a Gilbert damping $\alpha = 10^{-5}$, the strong coupling of the odd spin wave modes becomes evident from the transmission spectrum for $d = 1 \mu\text{m} \gg \lambda_{\text{ex}}$. In Fig. 3(a), anti-crossings occurs at $\omega_{\text{SWR}}^{(p)}$ with odd p that are marked by red dashed lines at the SWR magnetic fields $\mu_0 H_{\text{res}}^{(p)} \approx \left(-\omega_M - 2J\omega_M(p\pi/d)^2 + \sqrt{\omega_M^2 + 4\omega_{c,3}^2} \right) / (2\gamma)$. The satellite anti-crossings are absent in the TC model.

In Fig. 3(b), for $d = 5 \mu\text{m}$, the anti-crossing resonances of the lower spin wave modes condensate to the FMR splitting area. The coupling strengths decrease with increasing mode number as shown in Fig. 3(c). The magnon-photon coupling for the main $p = 1$ mode is proportional to the total magnetization, the coupling strength for spin waves $g^{(p)} \propto \sqrt{d}/p$ for pinned surface magnetizations, as shown in Fig. 3(d). For very thick films, i.e., $d > 2 \mu\text{m}$, the spin wave modes start to overlap and are difficult to distinguish. This collapse heralds the transition to the paramagnetic macrospin model in spite of the surface pinning. The lowest spin-wave mode is always dominant with \sqrt{d} -scaling that is not affected by the transition, as shown in the inset of Fig. 3(d).

C. Spin pumping

Spin pumping detected by the ISHE is a useful electrical technique to study magnetization dynamics [24]. Let us consider an ultrathin Pt film attached to the edge of the YIG slab as in Fig. 1(a). We assume free boundary conditions at the edges $y = 0$. The magnetization dynamics at the interface then injects a spin current into the Pt film that generates a Hall voltage $V_{\text{ISHE}} = D_{\text{ISHE}} j_s^{\text{sp}}$ over the Pt wire, with $D_{\text{ISHE}} \equiv (2e/\hbar)\theta\xi(d/\sigma d_y) \tanh(d_y/2\xi)$. We illustrate strong coupling in the V_{ISHE} spectrum here for the paramagnetic (unpinned macrospin) limit $J = 0$. The pumped spin current can be written

$$j_s^{\text{sp}} = \frac{\hbar g_r^{\uparrow\downarrow} \omega}{4\pi d M_s^2} \text{Im} \left[\left(u - \frac{v^2}{1+u} \right) \frac{iv^*}{1+u^*} \right] \int_{\frac{L-d}{2}}^{\frac{L+d}{2}} dx |\psi_3(x)|^2. \quad (14)$$

We assume that the Pt wire has the width $d_y = 10 \text{ nm}$ with conductivity $\sigma = 10^7 (\text{m} \cdot \Omega)^{-1}$, spin mixing conductance $g_r^{\uparrow\downarrow} = 10^{19} \text{ m}^{-2}$, spin Hall angle $\theta = 0.11$ and spin diffusion length $\xi = 1.5 \text{ nm}$ [36]. The spin back-flow contributes a minor correction that we disregard since $\xi \ll d_y$. The rf magnetic amplitude is chosen as $\mu_0 h_0 = 10 \mu\text{T}$. The microwave power absorption is defined as the integration of the Poynting vector enclosed by a section of the volume of the sample reads,

$$P_{\text{abs}} = \frac{\mu_0 d_y d_z \omega}{2} \text{Im} \left(u - \frac{v^2}{1+u} \right) \int_{\frac{L-d}{2}}^{\frac{L+d}{2}} dx |\psi_3(x)|^2. \quad (15)$$

By substituting u and v , we find that $j_s^{\text{sp}}/P_{\text{abs}} \propto \omega_M(\omega_M + \omega_H)/\alpha[\omega^2 + (\omega_M + \omega_H)^2]$ is almost a constant near the resonance, which proves that the spin pumping is a reliable measure of the microwave absorption. V_{ISHE} as a function of rf

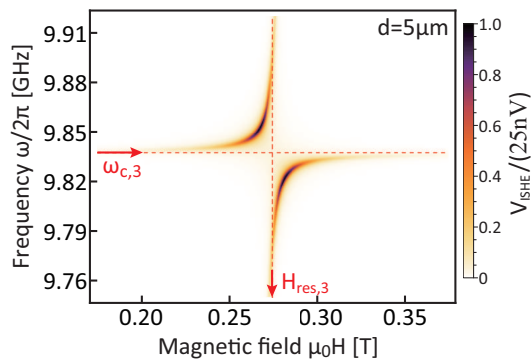


FIG. 4. Inverse spin Hall voltage spectrum. For a cavity $\ell/L = 2$, Gilbert damping $\alpha = 2 \times 10^{-3}$, and $J = 0$ (paramagnetic limit).

frequency and magnetic field is shown in Fig. 4 for film thickness $d = 5 \mu\text{m}$. In the present symmetric configuration there are no surface states that might interact strongly with the Pt contact [24, 37]. The calculations in the presence of exchange (not shown) support our conclusions.

IV. CONCLUSIONS

To summarize, we develop a scattering theory to study exchange magnon-polaritons, i.e., the hybridized magnetization and microwave dynamics, beyond the paramagnetic/macros spin and RWA that are implicit in the TC model. Our method and scattering coefficient Eq. (9) are valid for the full parameter range spanning the weak to strong coupling limits. The conventional input-output formula Eq. (1) is valid for odd cavity modes and only to leading order in the film thickness d , otherwise the cavity properties are strongly modified by the load. The exchange interaction between spins leads to strong coupling not only for the FMR mode but also for standing spin waves. The magnon-photon coupling depends on both the materials parameters and the spin wave mode index, e.g., decrease with increasing mode number. We confirm the transition from weak coupling, to strong coupling, to magnetically induced transparency and to ultra-strong coupling regimes. Spin pumping from magnon-polaritons into metallic thin film contacts shows pronounced anti-crossing spectra, which allows electric readout of magnon-photon states. We believe that our results will help to understand and engineer the coherent hybridization of ferromagnetic and superconducting order parameters in microwave cavities [16].

V. ACKNOWLEDGMENTS

We acknowledge helpful discussions with Yaroslav Blanter, Johannes Lotze, Hannes Maier-Flaig, Babak Zare Rameshti and Ka Shen. The research leading to these results has received funding from the European Union Seventh Framework Programme [FP7-People-2012-ITN] under grant agreement 316657 (SpinIcur). It was supported by JSPS Grants-in-Aid for Scientific Research (Grant Nos. 25247056, 25220910,

26103006), FOM (Stichting voor Fundamenteel Onderzoek der Materie), the ICC-IMR, EU-FET InSpin 612759, and DFG Priority Programme 1538 “Spin-Caloric Transport” (BA 2954/1, GO 944/4) and the collaborative research center SFB631 (C3).

- [1] Y. Kubo, F.R. Ong, P. Bertet, D. Vion, V. Jacques, D. Zheng, A. Dréau, J.F. Roch, A. Auffeves, F. Jelezko, J. Wrachtrup, M.F. Barthe, P. Bergonzo, and D. Esteve, *Phys. Rev. Lett.* **105**, 140502 (2010).
- [2] O.O. Soykal and M.E. Flatté, *Phys. Rev. Lett.* **104**, 077202 (2010); *Phys. Rev. B* **82**, 104413 (2010).
- [3] S. Putz, D.O. Krimer, R. Amsüss, A. Valookaran, T. Nöbauer, J. Schmiedmayer, S. Rotter, and J. Majer, *Nat. Phys.* **10**, 720 (2014).
- [4] B. Hillebrands and A. Thiaville (Eds.), *Spin Dynamics in Confined Magnetic Structures I*, (Springer-Verlag, Berlin, 2006).
- [5] D.L. Mills and E. Burstein, *Rep. Prog. Phys.* **37** 817 (1974).
- [6] A. Lehmeier and L. Merten, *J. Magn. Magn. Mater.* **50**, 32 (1985).
- [7] *Recent Advances in Magnetic Insulators - From Spintronics to Microwave Applications*, Solid State Physics, Vol. 64, edited by M. Wu and A. Hoffmann (Academic Press, 2013).
- [8] A.A. Serga, A.V. Chumak, and B. Hillebrands, *J. Phys. D: Appl. Phys.* **43**, 264002 (2010).
- [9] Y. Kajiwara, K. Harii, S. Takahashi, J. Ohe, K. Uchida, M. Mizuguchi, H. Umezawa, H. Kawai, K. Ando, K. Takanashi, S. Maekawa, and E. Saitoh, *Nature (London)* **464**, 262 (2010).
- [10] M. Gillett and S. Geller, *Phys. Rev.* **110**, 73 (1958).
- [11] D.I. Schuster, A.P. Sears, E. Ginossar, L. DiCarlo, L. Frunzio, J.J.L. Morton, H. Wu, G.A.D. Briggs, B.B. Buckley, D.D. Awschalom, and R.J. Schoelkopf, *Phys. Rev. Lett.* **105**, 140501 (2010).
- [12] E. Abe, H. Wu, A. Ardavan, and J.J.L. Morton, *Appl. Phys. Lett.* **98**, 251108 (2011).
- [13] H. Huebl, C.W. Zollitsch, J. Lotze, F. Hocke, M. Greifenstein, A. Marx, R. Gross, and S.T.B. Goennenwein, *Phys. Rev. Lett.* **111**, 127003 (2013).
- [14] G.B.G. Stenning, G.J. Bowden, L.C. Maple, S.A. Gregory, A. Sposito, R.W. Eason, N.I. Zheludev, and P.A.J. de Groot, *Opt. Exp.* **21**, 1456 (2013).
- [15] B. Bhoi, T. Cliff, I.S. Maksymov, M. Kostylev, R. Aiyar, N. Venkataramani, S. Prasad, and R.L. Stamps, *J. Appl. Phys.* **116**, 243906 (2014).
- [16] Y. Tabuchi, S. Ishino, T. Ishikawa, R. Yamazaki, K. Usami, and Y. Nakamura, *Phys. Rev. Lett.* **113**, 083603(2014); Y. Tabuchi, S. Ishino, A. Noguchi, T. Ishikawa, R. Yamazaki, K. Usami, and Y. Nakamura, arXiv:1410.3781v1.
- [17] X. Zhang, C.L. Zou, L. Jiang, and H.X. Tang, *Phys. Rev. Lett.* **113**, 156401 (2014).
- [18] M. Goryachev, W.G. Farr, D.L. Creedon, Y. Fan, M. Kostylev, and M.E. Tobar, *Phys. Rev. Applied*, **2**, 054002 (2014).
- [19] J.M. Fink, R. Bianchetti, M. Baur, M. Göppel, L. Steffen, S. Filipp, P.J. Leek, A. Blais, and A. Wallraff, *Phys. Rev. Lett.* **103**, 083601 (2009).
- [20] D.F. Walls and G.J. Milburn, *Quantum Optics* (Springer, 2008).
- [21] I. Chiorescu, N. Groll, S. Bertaina, T. Mori, and S. Miyashita, *Phys. Rev. B* **82**, 024413 (2010).
- [22] S. Agarwal, S.M.H. Rafsanjani, and J.H. Eberly, *Phys. Rev. A* **85**, 043815 (2012).

- [23] Y. Tserkovnyak and A. Brataas, and G.E.W. Bauer, Phys. Rev. B **66**, 224403 (2002); Y. Tserkovnyak, A. Brataas, G.E.W. Bauer, and B.I. Halperin, Rev. Mod. Phys. **77**, 1375 (2005).
- [24] C.W. Sandweg, Y. Kajiwara, K. Ando, E. Saitoh, and B. Hillebrands, Appl. Phys. Lett. **97**, 252504 (2010).
- [25] A. Hoffmann, IEEE Trans. Magn. **49**, 5172 (2013).
- [26] M. Weiner, J. Appl. Phys. **43**, 1246 (1972).
- [27] T.J. Gerson and J.S. Nadan, IEEE Trans. Microw. Theory Techn. **22**, 757 (1974).
- [28] R. Ruppin, J. Appl. Phys. **62**, 11 (1987).
- [29] K. Sadhana, R.S. Shinde, and S.R. Murthy, Int. J. Mod. Phys. B **23**, 3637 (2009).
- [30] S.A. Manuilov, S.I. Khartsev, and A.M. Grishin, J. Appl. Phys. **106**, 123917 (2009).
- [31] B. Heinrich, C. Burrowes, E. Montoya, B. Kardasz, E. Girt, Y.-Y. Song, Y. Sun, and M. Wu, Phys. Rev. Lett. **107**, 066604 (2011).
- [32] H. Kurebayashi, O. Dzyapko, V.E. Demidov, D. Fang, A.J. Ferguson, and S.O. Demokritov, Nat. Mater. **10**, 660 (2011).
- [33] C. Kittel, Phys. Rev. **110**, 1295 (1958).
- [34] H. Puzkarski, Prog. Surf. Sci. **9**, 191 (1979).
- [35] X. Liu, Y.Y. Zhou, and J.K. Furdyna, Phys. Rev. B **75**, 195220 (2007).
- [36] M. Weiler, M. Althammer, M. Schreier, J. Lotze, M. Pernpeintner, S. Meyer, H. Huebl, R. Gross, A. Kamra, J. Xiao, Y.-T. Chen, H.J. Jiao, G.E.W. Bauer, and S.T.B. Goennenwein, Phys. Rev. Lett. **111**, 176601 (2013).
- [37] A. Kapelrud and A. Brataas, Phys. Rev. Lett. **111**, 097602 (2013).